*energies*

MDPI

*Article*

# Paleoenvironment and Hydrocarbon Potential of Salinized Lacustrine Shale with High Terrigenous Input in the Paleogene Biyang Depression (East China): Evidence from Organic Petrography and Geochemistry

**Yu Song [1,2,3,*], Paerzhana Paerhati [3], Shilin Xu [1,2,4], Shu Jiang [3,*], Bo Gao [1,2], Shuifu Li [3], Qiang Cao [3], Zhonghui Li [3], Li Wan [3] and Chuang Li [3]**

1 State Key Laboratory of Shale Oil and Gas Enrichment Mechanisms and Efficient Development, Beijing 100083, China
2 Sinopec Key Laboratory of Shale Oil/Gas Exploration and Production Technology, Beijing 100083, China
3 Key Laboratory of Tectonics and Petroleum Resources, China University of Geosciences, Ministry of Education, Wuhan 430074, China; lc271531@163.com (C.L.)
4 Sinopec Petroleum Exploration and Production Research Institute, Beijing 100083, China
* Correspondence: songyu@cug.edu.cn or songyu1009@126.com (Y.S.); jiangsu@cug.edu.cn (S.J.)

**Abstract:** Salinized lacustrine shale (SLS) represents a frontier in the global quest for unconventional hydrocarbon resources. The impact of terrigenous input, which includes terrigenous organic matter (OM) and detrital matter, on the deposition and hydrocarbon potential of SLS is still controversial. Here, we examine this issue using the newly discovered SLS within the Paleogene Biyang Depression, employing a combination of organic petrographic and geochemical analyses. A high influx of terrigenous input (terrigenous OM and detrital matter) promotes the formation of SLS. On the one hand, terrigenous higher plants emerge as the primary source of OM in the SLS, as indicated by the dominance of terrigenous macerals (e.g., terrigenous liptinite) and the abundance of plant-derived biomarkers (e.g., tricyclic terpanes). Additionally, a portion of the OM may originate from bacteria. On the other hand, the rapid input of detrital matter improves the preservation of OM, resulting in the deposition of SLS with high total organic carbon (TOC) contents and low hydrogen index (HI) values. The findings of this study contribute to a deeper understanding of SLS deposition and provide guidance for regional hydrocarbon exploration.

**Keywords:** lacustrine organic-rich shale; paleo-saline lake; biomarkers; elemental geochemistry; deep resource exploration

check for updates

**Citation:** Song, Y.; Paerhati, P.; Xu, S.; Jiang, S.; Gao, B.; Li, S.; Cao, Q.; Li, Z.; Wan, L.; Li, C. Paleoenvironment and Hydrocarbon Potential of Salinized Lacustrine Shale with High Terrigenous Input in the Paleogene Biyang Depression (East China): Evidence from Organic Petrography and Geochemistry. *Energies* **2024**, *17*, 3003. https://doi.org/10.3390/en17123003

Academic Editor: Richard Coffin

Received: 11 May 2024
Revised: 1 June 2024
Accepted: 3 June 2024
Published: 18 June 2024

**Copyright:** © 2024 by the authors. Licensee MDPI, Basel, Switzerland. This article is an open access article distributed under the terms and conditions of the Creative Commons Attribution (CC BY) license (https://creativecommons.org/licenses/by/4.0/).

## 1. Introduction

With the growing demand for energy and the dwindling conventional oil reserves, both the exploration and exploitation of unconventional oil reservoirs become imperative. Among these, salinized lacustrine shale systems stand out for their distinct characteristics, presenting both challenges and opportunities for oil exploration and exploitation [1,2]. Salinity exerts a profound influence on sedimentation, diagenesis, and organic matter preservation, ultimately shaping the composition and distribution of hydrocarbon resources [3]. As such, unravelling the complex relationships between organic matter, depositional environments, and hydrocarbon potential in salinized lacustrine shale is essential for resource assessment and exploration strategies [4]. Note that the term 'shale' in this study refers to fine-grained sediments include clay particles (<4 μm), with varying proportions of silt-sized floating grains (up to 62.5 μm) of biogenic and detrital origin [5,6].

Salinized lacustrine shale was extensively deposited during the Paleogene period worldwide, with examples including the Green River Formation of Wyoming in the United States [1]; the Salt IV Formation of the Mulhouse Basin [7] and the Bituminous Limestone

of the Camargue Basin in France [8]; the Brown Shale Formation of the Central Sumatra Basin in Indonesia [9]; the Xiaganchaigou Formation of the Qaidam Basin in Northwestern China [10]; and the Kongdian and Shahejie formations of the Bohai Bay Basin [11,12], the Qianjiang Formation of the Jianghan Basin [13], the Funing Formation of the Subei Basin (Eastern China) [14], and the Hetaoyuan Formation of the Nanxiang Basin in Eastern China [15]. Many of these salinized lacustrine shales are renowned for their potential as prolific hydrocarbon source rocks, as well as sources and reservoirs for shale oil resources [4]. Saline lacustrine basins harbor diverse biological organisms and demonstrate significant biological activities. This activity plays a role in enriching the sedimentary organic matter within the basins. The enrichment process includes biological bloom, primary productivity, water stratification, and organic matter preservation. Water stratification in saline lacustrine basins facilitates the preservation of sedimentary organic matter by inducing bottom water anoxia [16].

The Biyang Depression within the Nanxiang Basin represents the first shale oil breakthrough in Eastern China. The Well BYHF1, situated at the center of the depression, achieved a peak daily oil production of 24.2 tons [17]. However, oil production from the well declined rapidly, dropping to less than 5 tons per day after only 100 days [18]. Aside from potential hydraulic fracturing difficulties, the heterogeneity of salinized lacustrine shale is a major contributor to the rapid decline in production [19]. Consequently, in recent years, alongside shale oil exploration and exploitation in the $Eh_3^3$ and $Eh_3^2$ strata, which contain salinized lacustrine shale with the highest quality and the largest thickness, preliminary exploration of deeper shale strata (e.g., $Eh_3^6$ and $Eh_3^5$) in the depression is also planned [19]. However, there is still a lack of studies on organic matter source, depositional environment, and hydrocarbon potential for these deeper shale strata, significantly impending further shale oil exploration efforts in the Biyang Depression.

This article presents the results of a comprehensive organic petrographic and geochemical study conducted on the newly explored, deeper salinized lacustrine shale strata in the Paleogene Biyang Depression. Through integrated analyses, our objective was to elucidate the origin of organic matter, characterize the depositional environment of the shale strata, and assess their implications for hydrocarbon prospectivity. The findings of this study not only contribute to the understanding of salinized lacustrine shale systems in East China but also provide valuable insights into hydrocarbon exploration and resource assessment in similar geological settings worldwide.

## 2. Geological Setting

The Nanxiang Basin, situated in East China, is a sedimentary rift basin covering approximately $1.7 \times 10^4$ km$^2$ (Figure 1A). It includes the Xiangzao, Nanyang, and Biyang depressions, as well as the Shigang, Xinye, Tanghe, and Sheqi uplifts (Figure 1B). The hydrocarbon-rich Biyang Depression spans nearly 1000 km$^2$ and boasts conventional oil reserves of 306 million tons and shale oil reserves of 285 million tons [16,20]. The depression takes the form of a half-graben rift, further divided into the northern slope belt, central deep sag, and southern steep slope belt (Figure 1C,D).

There are four distinct episodes that comprise the structural evolution of a depression. (Episodes I−IV; Figure 2) [21–23]. Episode I signifies the early initial rifting stage, extending from the Paleocene to the very Early Eocene. The Yuhuangding Formation (Ey) was deposited during this phase, characterized by the prevalence of yellow-to-red coarse-grained sandstone interbedded with mudstone, suggesting fluvial facies. Episode II represents the late initial rifting stage and aligns with the deposition of the Early Eocene Dacangfang Formation (Ed). The Ed is marked by an abundance of purple-red coarse- and medium-grained sandstone and grey mudstone, with the occurrence of gypsum at the top, deposited in semi-saline lacustrine environments. The peak of the rifting stage, Episode III, spans the Middle-to-Late Eocene and is denoted by the third and second members of the Hetaoyuan Formation ($Eh_3$ and $Eh_2$). The $Eh_3$ mainly comprises grey-to-dark-grey shale interbedded with carbonate rock, deposited in deep-to-semi-deep saline lacustrine envi-

ronments. The $Eh_2$ consists of greyish-green-to-light-grey mudstone, carbonate rock, and fine-grained sandstone, indicating shallow lacustrine environments. Trona is occasionally found interbedded with dolostone in both the upper $Eh_3$ and $Eh_2$. The late rifting stage, Episode IV during the Oligocene, coincides with the deposition of the first member of the Hetaoyuan Formation ($Eh_1$) and the Liaozhuang Formation (El). The $Eh_1$ exhibits greyish-green-to-light-grey mudstone interbedded with medium and fine sandstone, suggesting shoreline shallow lake environment. The El is characterized by brown-red fine-grained sandstone, mudstone, and gypsum, signifying a transition from a riverine environment to a saline-lake environment.

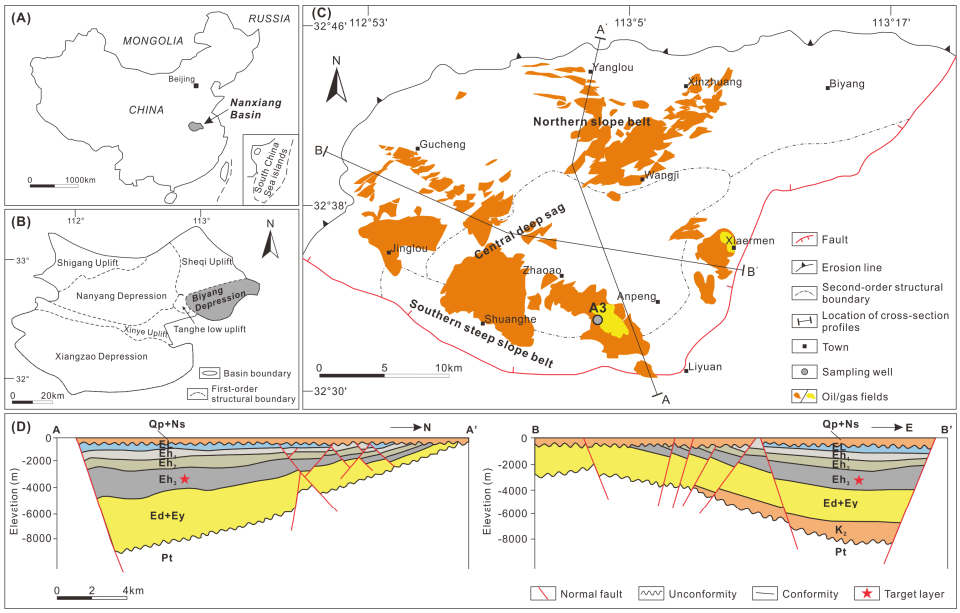



**Figure 1.** (**A**) Location of the Nanxiang Basin in East China. (**B**) Division of structural units in the Nanxiang Basin and location of the Biyang Depression. (**C**) Division of structural units in the Biyang Depression with locations of discovered oil/gas fields and the sampling well A3. (**D**) Profiles illustrating the vertical structures of the Biyang Depression. Locations for the profiles are given in (**C**). El = the Liaozhuang Formation; $Eh_{1,2,3}$ = first, second, and third member of the Hetaoyuan Formation; Ey = the Yuhuangding Formation; $K_2$ = Lower Cretaceous; $P_t$ = Permian–Triassic.

The $Eh_3$ interval is further subdivided into eight units, denoted as Unit VIII to Unit I from bottom to top ($Eh_3^8$ to $Eh_3^1$; Figure 2). This study focuses on the Units VI and V ($Eh_3^6$ and $Eh_3^5$), deposited in a deep/semi-deep lake, which comprises salinized lacustrine shale, and they have been prominent targets in recent hydrocarbon exploration efforts [20].

## 3. Materials and Methods

In the exploration well A3, a total of twenty fine-grained sediments were collected from depths ranging from 3195.2 to 3383.6 m, which is located in the southern part of the central deep sag (Figure 1C). All samples were analyzed for total organic carbon (TOC; wt. %) and Rock-Eval pyrolysis. A Leco CS-230 instrument (LECO Corporation, St. Joseph, MI, USA) was employed to determine the TOC contents after the acidification of samples to eliminate carbonate. A Rock-Eval 6 instrument (Vinci Technologies, Nanterre, France) was used for characterizing free hydrocarbons ($S_1$; mg HC/g rock), hydrocarbons cracked from kerogen ($S_2$; mg HC/g rock), and the maximum temperature of hydrocarbon generation ($T_{max}$; °C).

Ten samples were selected for the organic petrographic analysis. Polished sections were observed using a Nikon microscope (Nikon Corporation, Tokyo, Japan) equipped with reflected and fluorescent light, as well as 20× and 50× oil-immersion lenses. Mean random vitrinite reflectance of six samples was determined in accordance with an established procedure [24].

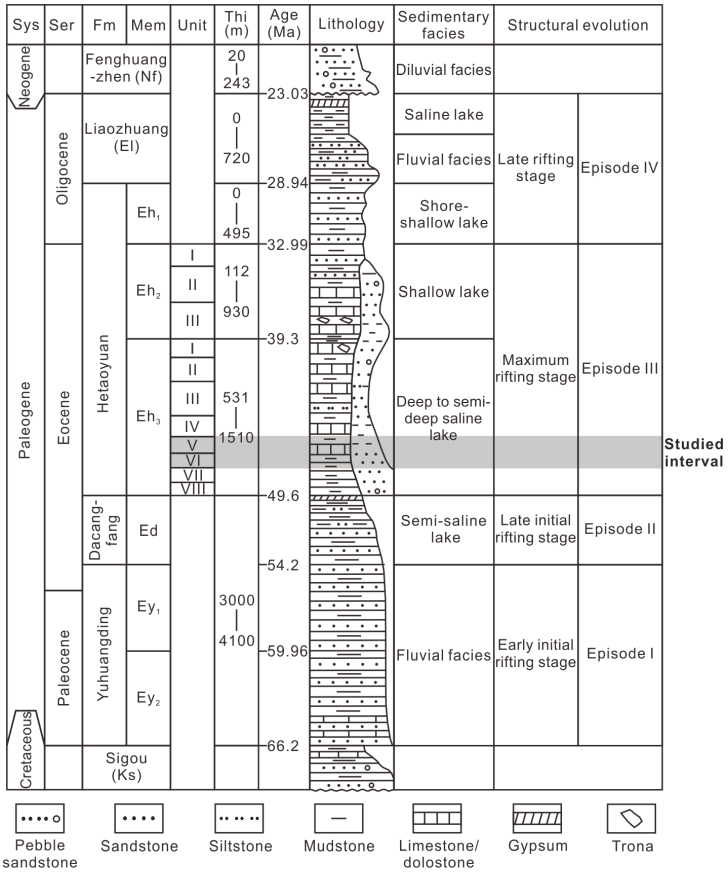



**Figure 2.** Stratigraphic section, sedimentary facies, and structural evolution of the Biyang Depression. Sys = system, Ser = series, Fm = formation, Mem = member, and Thi = thickness.

Major and trace elemental compositions were analyzed in 19 samples. The determination of major-element oxide contents was conducted using a Shimadzu XRF-1800 instrument (Shimadzu, Kyoto, Japan), while a Thermo Fisher Scientific Element XR ICP-MS (Thermo Fisher Scientific, Waltham, MA, USA) was used to determine the concentration of trace elements. To ensure analytical reliability, both standard materials and duplicate determination of samples were employed.

A total of 11 samples underwent biomarker analysis in this study. Initially, powdered samples were subjected to 72-h extraction with chloroform. Asphaltenes were then precipitated from an 80:1 (*v*:*v*) solution of hexane and dichloromethane (DCM) and subsequently separated via centrifugation. Soluble components of hexane were further divided into saturates, aromatics, and NSO compounds by silica gel and alumina column chromatography ($Al_2O_3$). This separation process involved successive elution with hexane, a DCM–hexane solution (2:1, *v*:*v*), DCM, and methanol (MeOH). Subsequently, the saturated and aromatic fractions were subjected to analysis using a gas chromatograph equipped with a 30 m DB-5MS fused silica column (inner diameter 0.25 mm; film thickness 0.25 μm) coupled to an Agilent 7890-5977B gas chromatography–mass spectrometry (GC-MS) system (Agilent, America). The oven temperature was programmed to increase from 70 °C to 300 °C at a rate of 3 °C/min, followed by an isothermal period lasting 30 min. The mass spectrometer operated in the electron ionization mode, covering a scan range from mass to charge (*m*/*z*) of 50 to *m*/*z* 650, with a total scan time of 0.7 s.

## 4. Results

### *4.1. Bulk Geochemistry*

The $Eh_3^5$ shale contains TOC contents ranging from 0.3 wt. % to 1.8 wt. %, which is lower than that of the $Eh_3^6$ shale (0.8−2.2 wt. %; Table 1). The $S_1$+$S_2$ values span 1.3−2.5 mg

HC/g rock and 0.5−4.1 mg HC/g rock in the $Eh_3^6$ and $Eh_3^5$ shale, respectively. The hydrogen index (HI = 100 × $S_2$/TOC) exhibits low values in the $Eh_3^6$ shale (71−119 mg HC/g TOC) and high values in the $Eh_3^5$ shale (100−166 mg HC/g TOC). A comparable range of $T_{max}$ values are observed in the $Eh_3^6$ and $Eh_3^5$ shale, ranging from 439 to 462 °C and from 431 to 456 °C, respectively. Type $II_2$ kerogen predominates in the $Eh_3^5$ shale, while type III kerogen dominates the $Eh_3^6$ shale, according to cross-plots of HI versus $T_{max}$ and $S_2$ versus TOC (Figure 3).

**Table 1.** Bulk geochemical parameters, maceral compositions, vitrinite reflectance, and elemental ratios for the Eh36 and Eh35 shale from the Biyang Depression.

| Strata | Depth (m) | TOC (wt. %) | $S_1 + S_2$ (mg/g) | HI (mg/g TOC) | $T_{max}$ (°C) | PI | OSI (mg/g TOC) | Maceral Compositions (vol. %) | | | | | $10^2 \times$ P/Al | $Ba_{bio}$ | B/Ga | Sr/Ba | $U_{EF}$ | $M_{oEF}$ | $T_iO_2$ | $Al_2O_3$ |
|---|---|---|---|---|---|---|---|---|---|---|---|---|---|---|---|---|---|---|---|---|
| | | | | | | | | Telalg | Ter Lip | Lipto | Vitr | Iner | | | | | | | | |
| $Eh_3^5$ | 3195.2 | 1.0 | 1.8 | 149 | 456 | 0.18 | 33 | 0.3 | 0.7 | 0.1 | 0.9 | 0.6 | | | | | | | | |
| | 3196.2 | 0.8 | 1.6 | 162 | 448 | 0.19 | 37 | | | | | | 2.0 | 241 | 1.0 | 2.7 | 4.2 | 8.6 | 0.65 | 15.3 |
| | 3205.9 | 0.6 | 1.2 | 130 | 452 | 0.29 | 52 | | | | | | 0.7 | 181 | 0.5 | 2.5 | 1.7 | 2.1 | 0.73 | 17.7 |
| | 3206.5 | 0.8 | 1.6 | 148 | 442 | 0.31 | 65 | 0.1 | 0.2 | 0.2 | 0.4 | 0.1 | 0.8 | 238 | 0.9 | 2.6 | 1.6 | 4.3 | 0.62 | 14.4 |
| | 3207 | 0.4 | 0.7 | 123 | 455 | 0.37 | 71 | | | | | | 1.0 | 285 | 2.6 | 3.5 | 3.2 | 1.5 | 0.28 | 6.7 |
| | 3208.5 | 0.9 | 1.7 | 142 | 451 | 0.24 | 44 | 0.3 | 0.2 | 0.1 | 0.5 | 0.4 | 0.7 | 353 | 1.5 | 2.8 | 2.8 | 4.4 | 0.46 | 10.5 |
| | 3209.7 | 1.3 | 2.8 | 166 | 455 | 0.22 | 46 | 0.4 | 0.0 | 0.1 | 1.1 | 0.6 | 1.4 | 82 | 0.9 | 3.8 | 3.7 | 8.9 | 0.59 | 16.1 |
| | 3210.2 | 1.8 | 4.1 | 162 | 444 | 0.28 | 62 | 0.8 | 0.8 | 0.2 | 1.9 | 0.8 | 2.4 | 298 | 0.8 | 2.1 | 4.3 | 18.4 | 0.65 | 15.7 |
| | 3212 | 0.6 | 1.0 | 126 | 447 | 0.18 | 27 | | | | | | 1.9 | 367 | 2.8 | 2.5 | 4.9 | 7.7 | 0.27 | 7.3 |
| | 3213 | 1.0 | 1.9 | 154 | 454 | 0.22 | 43 | | | | | | 1.3 | 125 | 0.5 | 2.6 | 3.5 | 4.9 | 0.76 | 18.4 |
| | 3214 | 0.3 | 0.5 | 100 | 431 | 0.39 | 63 | | | | | | 1.0 | 172 | 0.7 | 1.9 | 1.4 | 15.5 | 0.72 | 15.9 |
| | 3214.5 | 1.1 | 2.2 | 151 | 442 | 0.23 | 46 | | | | | | | 191 | 1.8 | 1.7 | 7.0 | 12.5 | 0.56 | 13.8 |
| $Eh_3^6$ | 3342.6 | 2.2 | 2.9 | 81 | 443 | 0.40 | 54 | | | | | | 0.8 | 57 | 0.8 | 3.1 | 3.8 | 19.8 | 0.60 | 14.8 |
| | 3342.7 | 2.0 | 2.3 | 71 | 442 | 0.37 | 42 | 0.3 | 0.6 | 0.1 | 1.6 | 0.7 | 1.1 | 46 | 0.6 | 4.6 | 3.6 | 28.6 | 0.66 | 15.7 |
| | 3349.2 | 1.5 | 2.0 | 93 | 445 | 0.29 | 39 | 0.2 | 0.2 | 0.2 | 1.2 | 0.6 | 0.9 | 87 | 1.7 | 5.4 | 5.2 | 34.0 | 0.53 | 13.4 |
| | 3349.6 | 1.6 | 2.5 | 98 | 459 | 0.35 | 54 | 0.3 | 0.5 | 0.2 | 2.0 | 0.5 | 0.8 | 277 | 1.0 | 3.2 | 2.7 | 12.2 | 0.66 | 12.5 |
| | 3357.2 | 1.2 | 1.8 | 111 | 462 | 0.28 | 43 | 0.1 | 0.2 | 0.2 | 0.7 | 0.5 | | 232 | 0.8 | 3.2 | 9.8 | 27.4 | 0.52 | 12.8 |
| | 3357.6 | 0.8 | 1.3 | 119 | 452 | 0.27 | 44 | | | | | | 1.1 | 15 | 1.1 | 2.8 | 4.4 | 24.3 | 0.65 | 15.7 |
| | 3382.8 | 1.4 | 2.1 | 91 | 459 | 0.38 | 55 | | | | | | 1.7 | 97 | 1.5 | 3.8 | 3.7 | 14.9 | 0.50 | 13.2 |
| | 3383.6 | 1.6 | 2.2 | 81 | 439 | 0.42 | 58 | 0.3 | 0.5 | 0.1 | 2.5 | 0.4 | 0.7 | 76 | 1.0 | 2.9 | 2.8 | 19.3 | 0.56 | 15.3 |

Tel = telalginite. Ter Lip = terrigenous liptinite. Lipto = liptodetrinite. Vitr = vitrinite. Iner = inertinite.

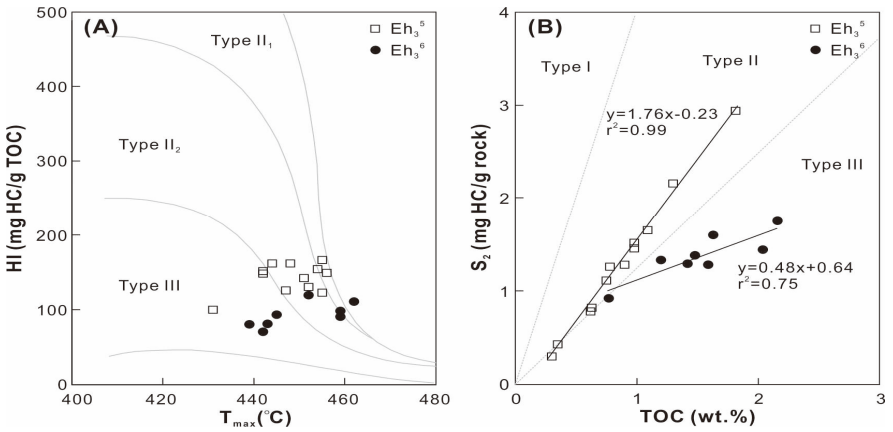



**Figure 3.** Cross-plots of (**A**) $T_{max}$ versus HI and (**B**) TOC versus $S_2$.

### *4.2. Organic Petrography and Vitrinite Reflectance*

The volume percentages (vol. %) of maceral in the $Eh_3^6$ and $Eh_3^5$ shale are less than 5.0 vol. % (Figure 4; Table 1). The $Eh_3^5$ shale contains a larger concentration of telalginite (including degraded telalginite) than the $Eh_3^6$ shale, resulting in higher HI values (Figure 3A). Telalginite appears as a unicellular spherical or almost-round shape with yellow-to-orange fluorescence (Figure 5A), whereas degraded telalginite has indistinct boundaries and diminished fluorescence (Figure 5B). Terrigenous liptinite, which is dominated by sporinite and cutinite, ranges from 0.2 to 0.6 vol. % and less than 0.1 to 0.8 vol. % in the $Eh_3^6$ and $Eh_3^5$ shale, respectively. Sporinite is distinguished by its elongated thread-like or fusiform shape with yellow-orange fluorescence, whereas cutinite has a serrated edge and poor fluorescent properties (Figure 5C). Both intervals contain trace amounts of liptodetrinite (<0.2 vol. %), which has a small and irregular shape with yellow fluorescence (Figure 5A,C). Among macerals, vitrinite is most prevalent, with values in the $Eh_3^6$ shale ranging from 0.7 to 2.5 vol. %, and in the $Eh_3^5$ shale from 0.4 to 1.9 vol. %. The spherical shape of vitrinite suggests that it may transport across long distances, probably suggesting deep-to-semi-deep lacustrine environments (Figure 5D). Inertinite is found in needle-shaped grains and

is most likely broken fusinite or semifusinite (Figure 5E). Furthermore, a minor amount of framboidal and semi-cube pyrite is observed, indicating that there were possibly different stages of pyrite formation (Figure 5F). The average values of random vitrinite reflectance (%Rr) vary between 0.9 and 1.0% (Figure 4; Table 1).

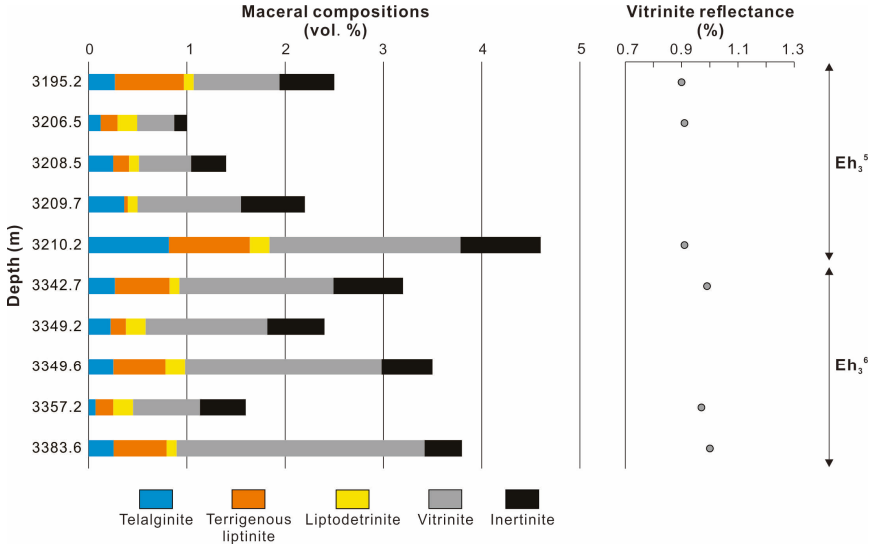



**Figure 4.** Vertical variations in maceral compositions and vitrinite reflectance.

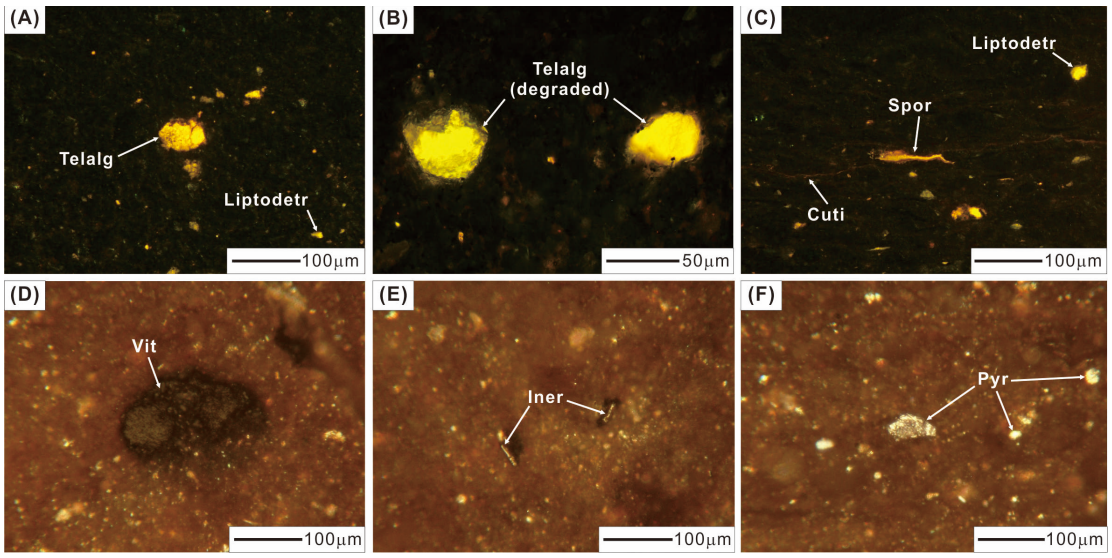



**Figure 5.** Representative photos of maceral. (**A**) Telalginite (Telalg) and liptodetrinite (Liptodetr), 3342.7 m, $Eh_3^6$. (**B**) Degraded telalginite, 3349.2 m, $Eh_3^6$. (**C**) Sporinite (Spor), cutinite (Cuti), and liptodetrinite, 3196.2 m, $Eh_3^5$. (**D**) Vitrinite (Vit), 3196.2 m, $Eh_3^5$. (**E**) Inertinite (Iner), 3196.2 m, $Eh_3^5$. (**F**) Pyrite (Pyr), 3357.2 m, $Eh_3^6$. (**A**–**C**) Under fluorescent light. (**D**–**F**) Under white incident light.

### *4.3. Elemental Compositions*

The elemental metrics used as paleoenvironmental indicators are listed in Table 1, including the P/Al ratio; biogenic Ba value ($Ba_{bio} = Ba_{tot} - Al \times (Ba/Al)_{detrital}$, where $Ba_{tot}$ and Al are the total amounts of Ba and Al, and $(Ba/Al)_{detrital}$ is estimated based on the cross-plot of Ba versus Al) [25]; Sr/Ba and B/Ga ratios; enrichment factors of U and Mo ($TE_{EF} = (TE/Al)_{sample}/(TE/Al)_{UCC}$ [26], where TE stands for the U or Mo concentrations, and UCC refers to elemental composition of the Upper Continental Crust) [27]; and $TiO_2$ and $Al_2O_3$ contents.

The 100 × P/Al ratios in the $Eh_3^6$ and $Eh_3^5$ shale range from 0.7 to 1.7 and from 0.7 to 2.4, respectively. The $Eh_3^6$ shale has $Ba_{bio}$ levels ranging from 15 to 277 ppm, which is less than the $Eh_3^5$ shale's range, which is from 82 to 367 ppm. The $Eh_3^6$ and $Eh_3^5$ shale have Sr/Ba ratios that range from 0.6 to 1.7 and from 0.5 to 2.8, respectively. The B/Ga ratios of the $Eh_3^6$ shale (2.8–5.4) are greater than those of the $Eh_3^5$ shale (1.7–3.8). The $U_{EF}$ and $Mo_{EF}$ values exhibit the same pattern, with higher values in the $Eh_3^6$ shale ($U_{EF}$: 2.7–9.8; $Mo_{EF}$: 12.2–34.0) and lower values in the $Eh_3^5$ shale ($U_{EF}$: 1.4–7.0; $Mo_{EF}$: 1.5–18.4). Regarding the $TiO_2$ and $Al_2O_3$ contents, the $Eh_3^6$ shale values range from 0.50 to 0.66 wt. % and from 12.5 to 15.7 wt. %, respectively, while in the $Eh_3^5$ shale, they range from 0.27 to 0.76 wt. % and from 6.7 to 18.4 wt. %, respectively (Figure 6).

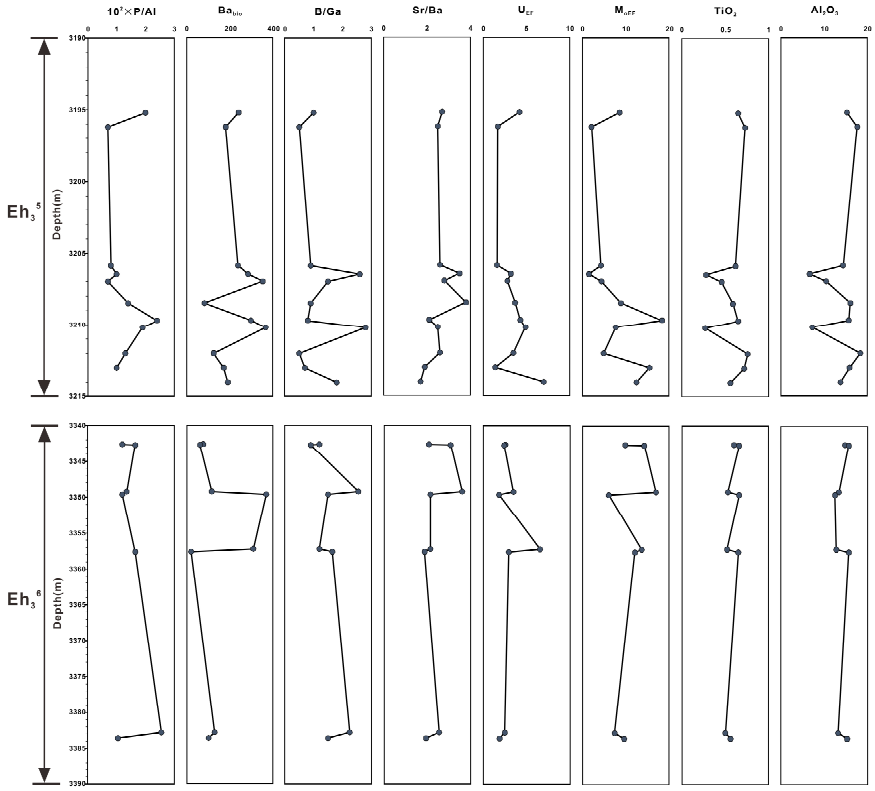



**Figure 6.** Vertical variations in elemental geochemical parameters of the $Eh_3^6$ and $Eh_3^5$ shale.

### *4.4. Biomarkers*

The $Eh_3^6$ and $Eh_3^5$ shale contain varying levels of chloroform bitumen 'A', ranging from 0.10 to 0.17 wt. % and from 0.08 to 0.16 wt. %, respectively (Table 2). The $Eh_3^6$ shale (87.1–94.4 wt. %) contains higher proportions of hydrocarbon fractions compared to the $Eh_3^5$ shale (82.0–88.2 wt. %). Both intervals exhibit a prevalence of saturated over aromatic fractions, with saturated/aromatic hydrocarbon ratios varying between 2.8 and 4.5.

The $Eh_3^6$ and $Eh_3^5$ shale are dominated by short-chain *n*-alkanes ($n$-$C_{17\text{-}23}$) with a predominance of odd over even (Figure 7A). The acyclic isoprenoid pristane (Pr) exhibits a higher abundance compared to phytane (Ph), with Pr/Ph ratios ranging from 0.87 to 1.01 in the $Eh_3^6$ shale and from 0.98 to 1.37 in the $Eh_3^5$ shale (Table 2). The $Eh_3^6$ shale has ratios of Pr/$n$-$C_{17}$ and Ph/$n$-$C_{18}$ that fall between 0.12 and 0.31 and between 0.17 and 0.32, respectively. On the other hand, the $Eh_3^5$ shale exhibits two ratios that vary from 0.36 to 0.51 (Pr/$n$-$C_{17}$) and from 0.29 to 0.38 (Ph/$n$-$C_{18}$), respectively. Drimanes, labdanes, methylheptadecanes, and b-carotane are also assigned in the TIC chromatogram (Figure 7A).

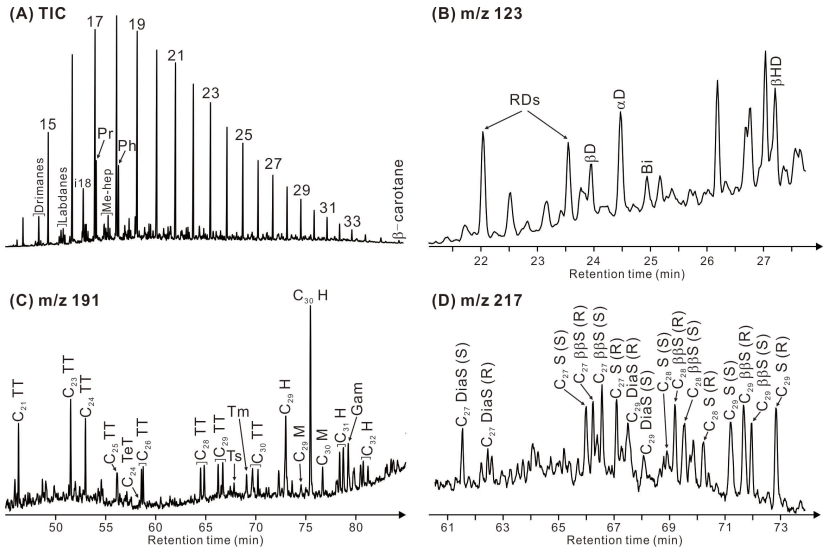



**Figure 7.** (**A**) Total ion current (TIC) chromatogram of saturated hydrocarbon fraction of a representative sample (3357.2 m, $Eh_3^6$). (**B**) Mass chromatogram (*m/z* 123) of the corresponding drimanes and bisabolane. (**C**) Mass chromatogram (*m/z* 191) of the corresponding terpenoids. (**D**) Mass chromatogram of the corresponding steranes. A key to labelled peaks in the chromatograms is provided in Table 3.

The mass chromatograms of drimanes (*m/z* 123; Figure 7B) reveal relatively high abundance of 8a(H)-drimane, followed by rearranged drimanes, 8β(H)-homodrimane, 8β(H)-drimane, and bisabolane. The $Eh_3^6$ shale has ratios ranging from 1.13 to 1.80 for rearranged drimanes/drimanes and from 1.66 to 2.28 for 8β(H)-homodrimane/8β(H)-drimane. In contrast, two ratios in the $Eh_3^5$ shale fall between 0.70 and 1.11 and between 1.43 and 1.71, respectively (Table 2).

The mass chromatograms of terpenoids (*m/z* 191; Figure 7C) illustrate that tricyclic terpanes are assigned within the range from $C_{21}$ to $C_{30}$ (excluding $C_{22}$ and $C_{27}$), along with $C_{24}$ tetracyclic terpane. Short-chain tricyclic terpanes (<$C_{24}$) are more abundant compared to their longer-chain homologues. The ratios of $C_{24}$ tetracyclic/$C_{26}$ tricyclic terpanes vary from 0.38 to 0.66 in the $Eh_3^6$ shale and from 0.21 to 0.38 in the $Eh_3^5$ shale (Table 2). The non-aromatic cyclic triterpenoids are primarily composed of hopanoids. The most abundant hopanoid is 17α, 21β $C_{30}$ hopane ($C_{30}$H), followed by 17a, 21β $C_{29}$ norhopane, 17α, 21β $C_{31\text{-}32}$ homohopane (22S+22R), 17β, 21α $C_{29\text{-}30}$ moretane, and 18α(H)-trisnorhopane (Ts) and 17α(H)-trisnorhopane (Tm). The ratios of Ts/(Ts+Tm) and $C_{31}$ homohopane 22S/(22S+22R) isomers range from 0.67 to 0.76 and from 0.58 to 0.61 in the $Eh_3^6$ shale, while in the $Eh_3^5$ shale, these ratios vary between 0.57 and 0.73 and between 0.57 and 0.61, respectively. Gammacerane (Ga) is also assigned in *m/z* 191 mass chromatograms, with Ga/$C_{30}$H ratios of 0.59–0.82 in the $Eh_3^6$ shale and 0.50–0.71 in the $Eh_3^5$ shale.

The mass chromatograms of terpenoids (*m/z* 191; Figure 7C) illustrate that tricyclic terpanes are assigned within the range from $C_{21}$ to $C_{30}$ (excluding $C_{22}$ and $C_{27}$), along with $C_{24}$ tetracyclic terpane. Short-chain tricyclic terpanes (<$C_{24}$) are more abundant compared to their longer-chain homologues. The ratios of $C_{24}$ tetracyclic/$C_{26}$ tricyclic terpanes vary from 0.38 to 0.66 in the $Eh_3^6$ shale and from 0.21 to 0.38 in the $Eh_3^5$ shale (Table 2). The non-aromatic cyclic triterpenoids are primarily composed of hopanoids. The most abundant hopanoid is 17α, 21β $C_{30}$ hopane ($C_{30}$H), followed by 17a, 21β $C_{29}$ norhopane, 17α, 21β $C_{31\text{-}32}$ homohopane (22S+22R), 17β, 21α $C_{29\text{-}30}$ moretane, and 18α(H)-trisnorhopane (Ts) and 17α(H)-trisnorhopane (Tm). The ratios of Ts/(Ts+Tm) and $C_{31}$ homohopane 22S/(22S+22R) isomers range from 0.67 to 0.76 and from 0.58 to 0.61 in the $Eh_3^6$ shale, while in the $Eh_3^5$ shale, these ratios vary between 0.57 and 0.73 and between 0.57 and 0.61, respectively. Gammacerane (Ga) is also assigned in *m/z* 191 mass chromatograms, with Ga/$C_{30}$H ratios of 0.59–0.82 in the $Eh_3^6$ shale and 0.50–0.71 in the $Eh_3^5$ shale.

**Table 2.** Chloroform bitumen 'A', group composition, and biomarker ratios for the Eh36 and Eh35 shale from the Biyang Depression.

| Strata | Depth (m) | A (wt. %) | B (wt. %) | C | D | E | F | G | H | I | J | K | L | M | N | O | P | Q | R (%) | S (%) | T (%) |
|---|---|---|---|---|---|---|---|---|---|---|---|---|---|---|---|---|---|---|---|---|---|
| $Eh_3^5$ | 3195.2 | 0.10 | 85.8 | 3.4 | 1.31 | 0.44 | 0.36 | 0.88 | 1.48 | 0.24 | 0.60 | 0.60 | 0.46 | 1.66 | 0.52 | 0.67 | 0.88 | 0.84 | 32 | 46 | 22 |
| | 3196.2 | 0.09 | 82.0 | 4.4 | 1.12 | 0.39 | 0.33 | 0.70 | 1.43 | 0.37 | 0.64 | 0.59 | 0.71 | 2.21 | 0.52 | 0.66 | 0.87 | 0.96 | 35 | 42 | 23 |
| | 3206.5 | 0.08 | 85.2 | 2.9 | 1.05 | 0.36 | 0.38 | 1.11 | 1.71 | 0.37 | 0.62 | 0.59 | 0.51 | 1.64 | 0.51 | 0.67 | 0.91 | 0.86 | 41 | 29 | 30 |
| | 3208.5 | 0.11 | 82.7 | 3.9 | 1.12 | 0.38 | 0.34 | 1.09 | 1.47 | 0.38 | 0.63 | 0.58 | 0.64 | 2.32 | 0.51 | 0.66 | 0.96 | 0.93 | 31 | 41 | 28 |
| | 3209.7 | 0.14 | 85.0 | 3.4 | 0.98 | 0.42 | 0.29 | 0.96 | 1.66 | 0.21 | 0.73 | 0.61 | 0.5 | 1.50 | 0.54 | 0.66 | 1.01 | 0.91 | 36 | 36 | 28 |
| | 3210.2 | 0.16 | 88.2 | 3.0 | 1.37 | 0.51 | 0.33 | 0.88 | 1.54 | 0.32 | 0.57 | 0.57 | 0.51 | 1.85 | 0.51 | 0.63 | 0.86 | 0.89 | 28 | 51 | 21 |
| $Eh_3^6$ | 3342.7 | 0.13 | 88.5 | 3.2 | 1.01 | 0.28 | 0.28 | 1.80 | 2.11 | 0.47 | 0.76 | 0.59 | 0.64 | 1.89 | 0.57 | 0.70 | 0.95 | 0.95 | 34 | 30 | 36 |
| | 3349.2 | 0.17 | 94.4 | 4.5 | 0.99 | 0.12 | 0.13 | 1.63 | 2.28 | 0.51 | 0.68 | 0.60 | 0.59 | 2.64 | 0.54 | 0.71 | 0.97 | 0.98 | 28 | 41 | 31 |
| | 3349.6 | 0.11 | 89.7 | 2.8 | 0.87 | 0.24 | 0.17 | 1.33 | 1.66 | 0.46 | 0.67 | 0.61 | 0.71 | 2.81 | 0.58 | 0.68 | 1.07 | 1.02 | 32 | 30 | 38 |
| | 3357.2 | 0.10 | 87.1 | 3.8 | 0.89 | 0.31 | 0.32 | 1.13 | 1.87 | 0.38 | 0.75 | 0.58 | 0.82 | 2.65 | 0.53 | 0.67 | 1.01 | 0.95 | 24 | 28 | 48 |
| | 3383.6 | 0.10 | 87.1 | 3.1 | 0.91 | 0.2 | 0.22 | 1.21 | 1.97 | 0.66 | 0.72 | 0.6 | 0.67 | 2.43 | 0.55 | 0.7 | 0.89 | 1.00 | 22 | 27 | 51 |

A = chloroform bitumen 'A'. B = sum of saturated and aromatic hydrocarbon fractions. C = saturated/aromatic hydrocarbons. D = Pr/Ph. E = Pr/*n*-$C_{17}$. F = Ph/*n*-$C_{18}$. G = rearranged drimanes/drimanes. H = 8β(H)-homodrimane/8β(H)-drimane. I = $C_{24}$ tetracyclic/$C_{26}$ tricyclic terpanes. J = Ts/(Ts+Tm). K = $C_{31}$ homohopane 22S/(22S+22R). L = gammacerane/ab $C_{30}$ hopane. M = ααα $C_{29}$/$C_{27}$ sterane (20R). N = ααα $C_{29}$ steranes 20S/(20S+20R). O = ββ/(ββ+αα) $C_{29}$ steranes. P = MPI-1. Q = TNR-2. R = fluorene. S = dibenzofuran. T = dibenzothiophene. The sum of fluorene, dibenzofuran, and dibenzothiophene is 100%.

**Table 3.** Abbreviations for labelled biomarker compounds in Figures 6 and 7.

| Figure | *m/z* | Abbreviation | Compound | Figure | *m/z* | Abbreviation | Compound |
|---|---|---|---|---|---|---|---|
| Figure 7A | TIC | 15-33 | $C_{15}$-$C_{33}$ *n*-alkanes | Figure 7D | 217 | $C_{27}$ ββS (S) | 5α,14β,17β-cholestane (20S) |
| | | i18 | $C_{18}$ *iso*-alkane | | | $C_{27}$ S (R) | 5α,14α,17α-cholestane (20R) |
| | | Pr | Pristane | | | $C_{28}$ S (S) | 24-methyl-5α,14α,17α-cholestane (20S) |
| | | Me-hep | Methylheptadecanes | | | $C_{28}$ ββS (R) | 24-methyl-5α,14β,17β-cholestane (20R) |
| | | Ph | Phytane | | | $C_{28}$ ββS (S) | 24-methyl-5α,14β,17β-cholestane (20S) |
| Figure 7B | 123 | RDs | Rearranged drimanes | | | $C_{28}$ S (R) | 24-methyl-5α,14α,17α-cholestane (20R) |
| | | βD | 8β-drimane | | | $C_{29}$ S (S) | 24-ethyl-5α,14α,17α-cholestane (20S) |
| | | αD | 8α-drimane | | | $C_{29}$ ββS (R) | 24-ethyl-5α,14β,17β-cholestane (20R) |
| | | Bi | Bisabolane | | | $C_{29}$ ββS (S) | 24-ethyl-5α,14β,17β-cholestane (20S) |
| | | βHD | 8β-homodrimane | | | $C_{29}$ S (R) | 24-ethyl-5α,14α,17α-cholestane (20R) |
| Figure 7C | 191 | $C_{21}$-$C_{30}$ TT | $C_{21}$-$C_{30}$ tricyclic terpanes | Figure 8A | TIC | TeMNs | Tetramethylnaphthalenes |
| | | $C_{24}$ TeT | $C_{24}$ tetracyclic terpane | | | Phe | Phenanthrene |
| | | Ts | 18α-trisnorhopane | | | $C_2$ Fls | $C_2$ fluorenes |
| | | Tm | 17α-trisnorhopane | | | $C_4$ Fls | $C_4$ fluorenes |
| | | $C_{29}$ H | 17α,21β-norhopane | | | MPs | Methylphenanthrenes |
| | | $C_{29}$ M | 17β,21α-norhopane | | | DMPs | Dimethylphenanthrenes |
| | | $C_{30}$ H | 17α,21β-hopane | | | TMPs | Trimethylphenanthrenes |
| | | $C_{30}$ M | 17β,21α-hopane | | | Chr | Chrysene |
| | | $C_{31}$ H | 17α,21β-homohopane (22S+22R) | | | MChrs | Methylchrysenes |
| | | Gam | Gammacerane | | | B[e]P | Benzo[e]pyrene |
| | | $C_{32}$ H | 17α,21β-bishomohopane (22S+22R) | Figure 8C | 168 | 3-MB | 3-methylbiphenyl |
| Figure 7D | 217 | $C_{27}$ DiaS (S/R) | 13α,17β-diacholestane (20S/20R) | | | 4-MB | 4-methylbiphenyl |
| | | $C_{27}$ S (S) | 5α,14α,17α-cholestane (20S) | Figure 8D | 170 | TMN | Trimethylnaphthalene |
| | | $C_{27}$ ββS (R) | 5α,14β,17β-cholestane (20R) | | | | |

The mass chromatograms of steroids (*m/z* 217; Figure 7D) indicate the highest abundance of $C_{29}$ regular steranes, followed by $C_{27}$ and $C_{28}$ regular steranes. The ratios of ααα $C_{29}/C_{27}$ sterane (20R) range from 1.89 to 2.64 in the $Eh_3^6$ shale and from 1.50 to 2.32 in the $Eh_3^5$ shale (Table 2). Within the range of $C_{27\text{-}29}$ regular steranes, the 5α,14β,17β(H) steranes (20S+20R) dominate over the 5α,14α,17α(H) steranes (20S+20R). The ratios of aaa $C_{29}$ steranes 20S/(20S+20R) and ββ/(ββ+αα) $C_{29}$ steranes fluctuate between 0.53 and 0.58 and between 0.68 and 0.71 in the $Eh_3^6$ shale, whereas the $Eh_3^5$ shale exhibits two ratios of 0.51–0.54 and 0.63–0.67, respectively. Additionally, minor proportions of 13α,17β $C_{27}$ diasteranes (20S+20R) are also assigned.

Phenanthrene (P) and its mono-, di-, and tri-methyl-substituted homologues (MP, DMP, and TMP) are the predominant aromatic compounds (Figure 8), followed by chrysene and its methyl-substituted homologues (MChr), benzo[e]pyrene (B[e]P), fluorene (F), methyl biphenyl (MB), dibenzofuran (DBF), tri- and tetra-methyl naphthalene (TMN, TeMN), and dibenzothiophene (DBT). The Methylphenanthrene Index 1 (MPI-1 = 1.89×(3-MP+2-MP)/[P+1.26×(9-MP+1-MP)]) [28] values in the $Eh_3^6$ and $Eh_3^5$ shale ranges from 0.89 to 1.07 and from 0.86 to 1.01, respectively (Table 2). The trimethylnaphthalene ratio-2 (TNR-2 = (2,3,6-TMN+1,3,7-TMN)/(1,3,5-TMN+1,3,6-TMN+ 1,4,6-TMN)) [29] values vary between 0.95 and 1.02 for the $Eh_3^6$ shale and between 0.84 and 0.93 for the $Eh_3^5$ shale. Considering F, DBF, and DBT as 100%, the $Eh_3^6$ shale has a larger percentage of DBT, but the $Eh_3^5$ shale has a higher concentration of DBF.

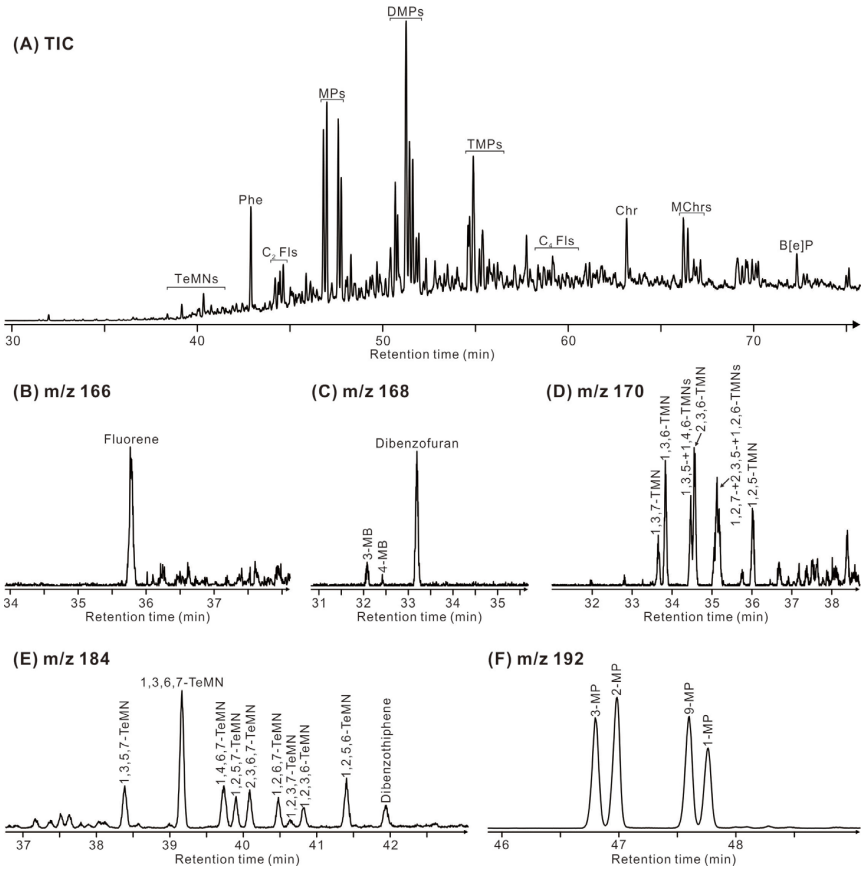



**Figure 8.** (**A**) Total ion current (TIC) chromatogram of aromatic hydrocarbon fraction of a representative sample (3196.2 m, $Eh_3^5$). (**B**) Mass chromatogram (*m/z* 166) of the corresponding fluorene. (**C**) Mass chromatogram (*m/z* 168) of the corresponding dibenzofuran and 3- and 4-methylbiphenyl. (**D**) Mass chromatogram (*m/z* 170) of the corresponding trimethylnaphthalene. (**E**) Mass chromatogram (*m/z* 184) of the corresponding tetramethylnaphthalene and dibenzothiophene. (**F**) Mass chromatogram (*m/z* 192) of the corresponding methylphenanthrene. A key to labelled peaks in the chromatograms is provided in Table 3.

## 5. Discussion

### *5.1. Maturity*

A peak oil window maturity is indicated by the mean values of random vitrinite reflectance (0.9–1.0%) for the $Eh_3^6$ and $Eh_3^5$ shale (Figure 4; Table 1). The conclusion is confirmed by the $T_{max}$ values, which are mainly distributed between 440 °C and 460 °C (Figure 3). Maturity indicators derived from terpenoids and steroids, including αβ $C_{31}$ homohopane 22S/(22S+22R), Ts/(Ts+Tm), ααα $C_{29}$ sterane 20S/(20S+20R), and ββ/(ββ+αα) $C_{29}$ steranes ratios, are close to the corresponding equilibrium values (Figure 9A,B), all of which suggest a maturity characteristic of the peak oil window [30]. Furthermore, aromatic maturity indicators like MPI-1 and TNR-2 confirm a maturity stage at the peak oil window (Figure 9C). Overall, the $Eh_3^6$ shale has greater MPI-1 and TNR-2 values than the $Eh_3^5$ shale, revealing a comparatively higher maturity. The peak oil window maturity is also evidenced by the presence of degraded telalginite (Figure 5B). Considering that the influences of thermal maturity on both intervals are comparable, paleoenvironmental biomarker indicators (e.g., Pr/Ph) are applied to contrast the paleoenvironmental differences between two intervals.

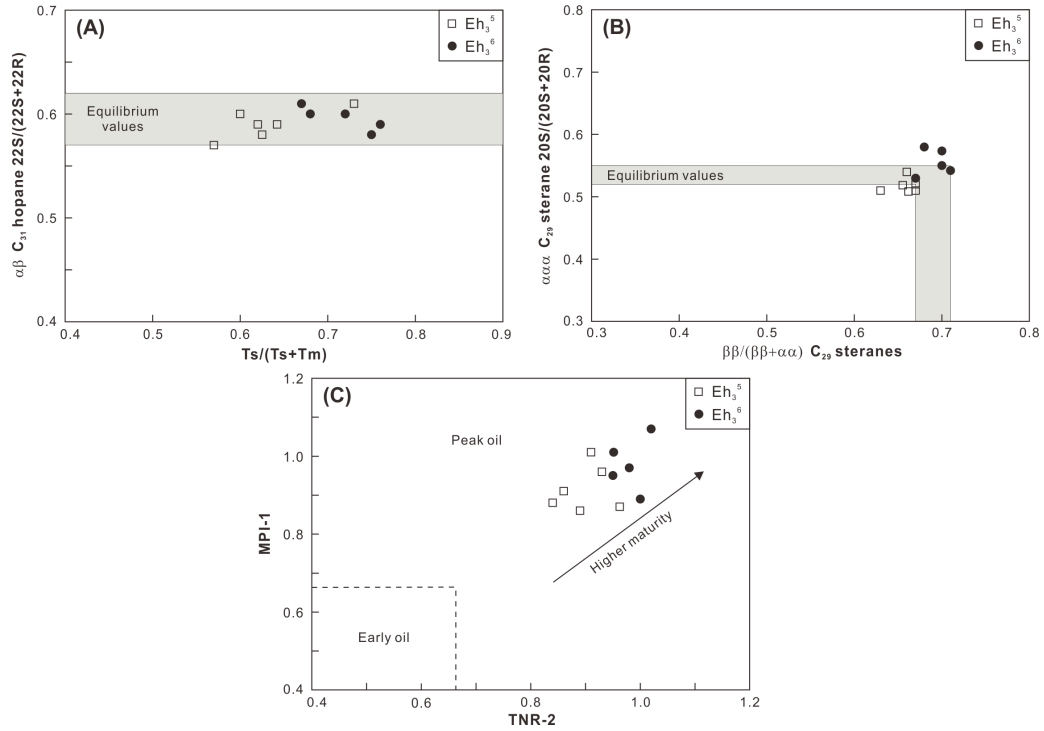



**Figure 9.** Cross-plots of (**A**) Ts/(Ts+Tm) versus αβ $C_{31}$ hopane 22S/(22S+22R), (**B**) ββ/(αα+ββ) $C_{29}$ steranes versus ααα $C_{29}$ sterane 20S/(20S+20R), and (**C**) TNR-2 versus MPI-1.

### *5.2. Organic Matter (OM) Source*

In contrast to the $Eh_3^3$ and $Eh_3^2$ shales, which exhibit a majority of type I-$II_1$ kerogen [15], the $Eh_3^6$ and $Eh_3^5$ shales display dominance by type $II_2$-III kerogen, suggesting that the organic matter is primarily derived from terrigenous higher plants (Figure 3). This inference is supported by the prevalence of terrigenous macerals (e.g., terrigenous liptinite, vitrinite, and inertinite) in both shale intervals, accounting for 82–91 vol.% (mmf = mineral matter free) and 68–85 vol.% (mmf) in the $Eh_3^6$ and $Eh_3^5$ shale, respectively. A negative correlation exists between the HI values and the contents of terrigenous macerals, indicating that the decreased HI values are associated with the increased contribution of higher plants (Table 1).

High ratios of $C_{24}$ tetracyclic/$C_{26}$ tricyclic terpanes ($C_{24}$ Tet/$C_{26}$ TT) are indicative of significant input of terrigenous OM [31]. The $Eh_3^6$ shale exhibits higher $C_{24}$ Tet/$C_{26}$ TT ratios compared to the $Eh_3^5$ shale, suggesting a substantial influx of terrigenous OM during

the shale's deposition (Figure 10A). It is commonly known that the main source of $C_{27}$ sterols is algae, whereas higher plants are usually linked to $C_{29}$ sterols. [32]. While some biomarker studies have revealed elevated levels of 24-ethylesterols in some microalgae species [33], the likelihood of microalgae-derived $C_{29}$ steranes can be ruled out in this case, given that OM is predominantly sourced from higher plants. Therefore, the elevated ratios of $C_{29}/C_{27}$ $\alpha\alpha\alpha$ steranes (20R) in the $Eh_3^6$ shale are consistent with the increased terrigenous OM input, which corroborates the findings of $C_{24}$ Tet/$C_{26}$ TT ratios (Figure 10A). Labdanes, which are typical higher plant-derived biomarkers [34], have also been assigned (Figure 7A), further confirming the contribution of terrigenous OM to the shale.

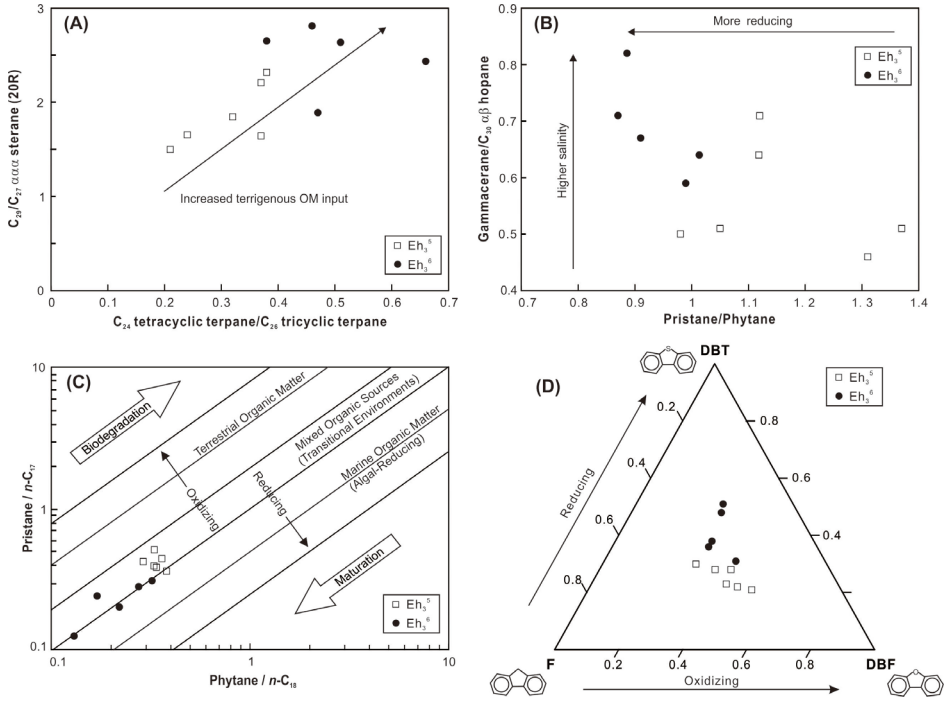



**Figure 10.** (**A**) Cross-plots of $C_{24}$ tetracyclic terpane/$C_{26}$ tricyclic terpane versus $C_{29}/C_{27}$ $\alpha\alpha\alpha$ sterane (20R). (**B**) Cross-plots of pristane/phytane versus gammacerane/$C_{30}$ αβ hopane. (**C**) Cross-plots of phytane/*n*-$C_{18}$ versus pristane/*n*-$C_{17}$. (**D**) Ternary plot of dibenzothiophene (DBT), fluorene (F), and dibenzofuran (DBF).

Furthermore, a portion of OM in shale may originate from bacteria, as indicated by the elevated concentrations of hopanoids (particularly αβ $C_{30}$ hopane) and the assignment of methylheptadecanes (Figure 7A,C) [35]. Hopanoids are mainly produced by prokaryotic organisms such as bacteria [36], whereas 7- and 8-methylheptadecanes are primarily generated by cyanobacteria and are found in significant concentrations in pure cultures of cyanobacteria [37].

### *5.3. Paleoenvironment Reconstruction*

In the middle of the Biyang Depression during the $Eh_3^6$ and $Eh_3^5$ periods, deep-to-semi-deep lacustrine environments were generally developed [20,22]. The integration of elemental compositions and biomarkers of shale reflects a variety of depositional environments, including paleosalinity, redox conditions, paleoproductivity, and detrital input. The B/Ga and Sr/Ba ratios, as well as the gammacerane index (GI = Ga/$C_{30}$H ratios), are utilized to infer paleosalinity levels. The B/Ga ratios range from 2.8 to 5.4 in the $Eh_3^6$ shale and from 1.7 to 3.8 in the $Eh_3^5$ shale, indicative of predominantly brackish and freshwater conditions, respectively (Figure 11A; based on the threshold proposed by [38]). This interpretation is corroborated by the higher GI values observed in the $Eh_3^6$ shale (0.59–0.82) compared to the $Eh_3^5$ shale (0.50–0.71; Figure 10B). However, the results derived from Sr/Ba ratios differ from those of the preceding parameters (Figure 11A). The impact of

carbonate-hosted Sr in the shale is thought to be the cause of this discrepancy, as indicated by a robust positive correlation between the CaO contents and Sr concentrations (the inset figure in Figure 11A).

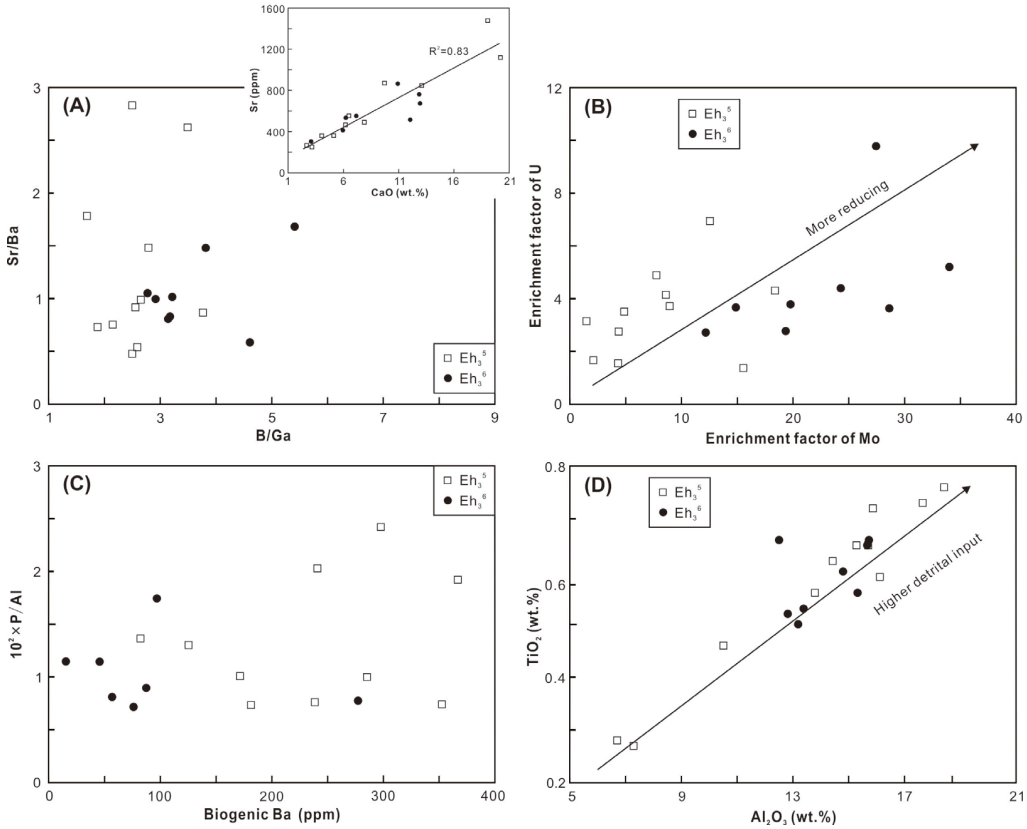



**Figure 11.** Cross-plots of (**A**) B/Ga versus Sr/Ba, with the inset figure showing CaO versus Sr; (**B**) enrichment factor of Mo versus enrichment factor of U; (**C**) biogenic Ba versus $10^2 \times$ P/Al; and (**D**) $Al_2O_3$ versus $TiO_2$.

The Pr/Ph ratios exhibit variability, ranging from 0.87 to 1.0 in the $Eh_3^6$ shale and 0.98 to 1.37 in the $Eh_3^5$ shale, suggesting the prevalence of more reducing conditions, probably anoxic (in accordance with the threshold proposed by [39]), during the deposition of $Eh_3^6$ shale (Figure 10B). Similarly, the cross-plot of Pr/*n*-$C_{17}$ versus Ph/*n*-$C_{18}$ indicates that the $Eh_3^6$ shale plots closer to the region representing reducing conditions (Figure 10C). Fluorene (F) tends to convert into dibenzofuran (DBF) under sufficient oxygen conditions, whereas it tends to generate dibenzothiophene (DBT) in oxygen-depleted conditions [40]. Thus, the positioning of shale in the ternary plot of DBT-F-DBF suggests that the $Eh_3^6$ shale was formed under comparatively more reducing conditions than the $Eh_3^5$ shale (Figure 10D). Furthermore, the enrichment factors of U and Mo, serving as redox proxies of sediments [41], also indicate the prevalence of more reducing conditions during the deposition of $Eh_3^6$ shale (Figure 11B).

The P/Al ratio and $Ba_{bio}$ value are applied to assess paleoproductivity. Overall, the $Eh_3^5$ shale exhibits high P/Al ratios and $Ba_{bio}$ values, whereas the $Eh_3^6$ shale displays comparatively low ratios and values (Figure 11C). These findings possibly suggest that the elevated paleoproductivity prevailed during the deposition of $Eh_3^5$ shale. However, this conclusion may raise questions, as an essential premise for utilizing P and Ba as productivity indicators is the predominance of aquatic-origin OM [42], which is evidently inconsistent with the studied shale. As discussed in Section 5.2, the primary source of OM is terrigenous higher plants, implying potentially low productivity of aquatic organisms. Therefore, it is postulated that aquatic productivity was low during the deposition of both intervals, potentially exerting limited influence on OM enrichment and shale formation.

Aluminum primarily originates from clay minerals, while titanium mainly occurs in clay and heavy minerals such as rutile. Clay minerals are abundant in both the $Eh_3^6$ and $Eh_3^5$ shale, whereas rutile is commonly found in the $Eh_3$ [19,22]. Therefore, the contents of Al and Ti are utilized to reveal detrital influx. The $Eh_3^6$ shale has a slightly higher average $Al_2O_3$ and $TiO_2$ concentration than the $Eh_3^5$ shale, suggesting an increased detrital supply to the paleo-lake during the deposition of $Eh_3^6$ shale.

The cartoons illustrating the depositional models of $Eh_3^6$ and $Eh_3^5$ shale are depicted in Figure 12. During the deposition of $Eh_3^6$ shale, there was a notable influx of detrital matter and terrigenous OM into the paleo-lake. Using 2000 Monte Carlo simulations of potential sedimentation rates, the earlier study performed an enhanced correlation coefficient (COCO) analysis for every member of $Eh_3$, resulting in high sediment accumulation rates (SARs), at 17.8 cm/kyr [23]. These high SARs facilitated the rapid burial of terrigenous OM, thus favoring its preservation. Moreover, because of the occurrence of gypsum at the top of the Ed and the relatively dry paleoenvironment, surface runoff may have transported salt ions released through the weathering of parent rock [43], leading to increased salinity in the paleo-lake and potentially promoting water stratification. Accordingly, the deposition of Eh36 shale, which has a high TOC and low HI value, was facilitated by the combination of a large terrigenous OM input and advantageous preservation circumstances (Figure 12A). In contrast, the deposition of $Eh_3^5$ shale was characterized by comparatively lower detrital matter and terrigenous OM, corresponding to lower SARs [23]. This lower terrigenous OM input, in conjunction with freshwater and suboxic conditions, resulted in the deposition of $Eh_3^5$ shale with low TOC and relatively higher HI values (Figure 12B).

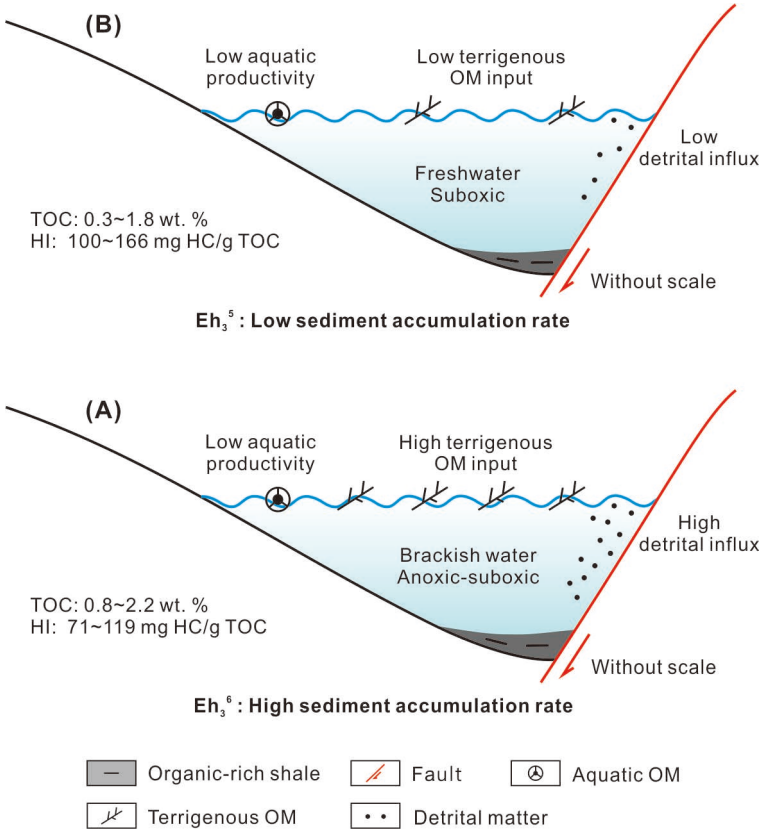



**Figure 12.** Depositional models of the (**A**) $Eh_3^6$ shale and (**B**) $Eh_3^5$ shale.

### *5.4. Hydrocarbon Potential and Implications for Regional Hydrocarbon Exploration*

The hydrocarbon generation potential of the $Eh_3^6$ and $Eh_3^5$ shale was evaluated using the cross-plot of TOC versus $S_1$+$S_2$ [44]. The $Eh_3^6$ shale falls within the region characterized by fair potential, whereas the $Eh_3^5$ shale predominantly exhibits poor-to-fair potential

(Figure 13A). This observation is further corroborated by the cross-plot of TOC versus HI, where the $Eh_3^6$ shale demonstrates fair oil potential, while the $Eh_3^5$ shale exhibits little-to-fair oil potential (Figure 13B). The hydrocarbon retention potential of the $Eh_3^6$ and $Eh_3^5$ shale is assessed through the cross-plots of TOC versus $S_1$ and production index (PI = $S_1/(S_1+S_2)$) versus oil saturation index (OSI = 100 × $S_1$/TOC). In these figures, comparatively higher contents of free (or migrated) hydrocarbons are evident in the $Eh_3^6$ shale compared to the $Eh_3^5$ shale (Figure 13C,D).

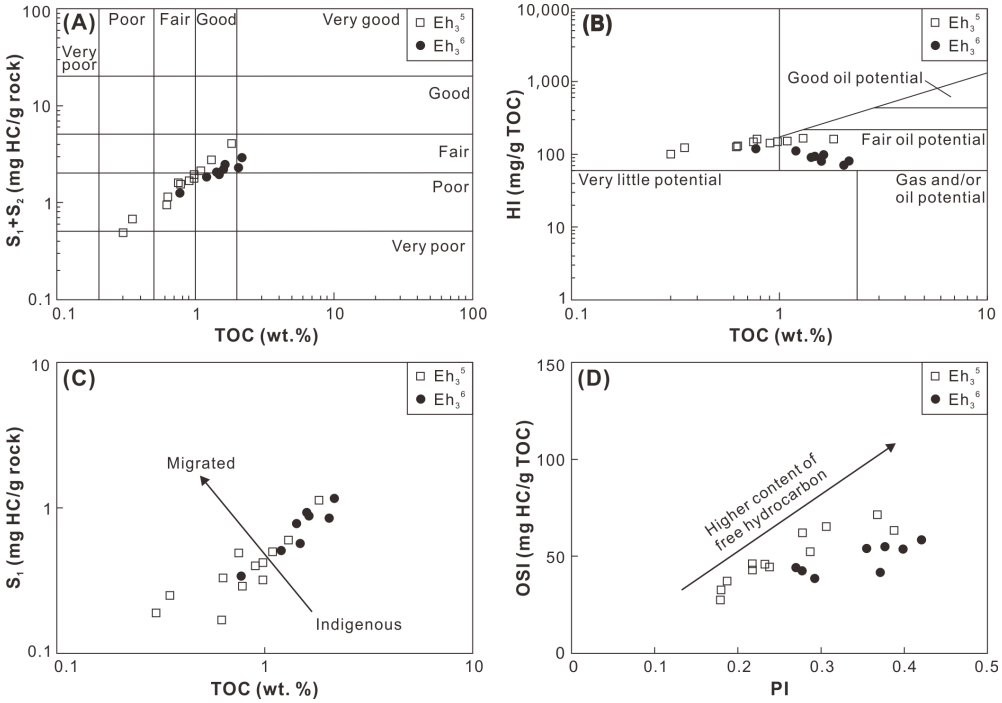



**Figure 13.** Cross-plots of (**A**) TOC versus $S_1+S_2$, (**B**) TOC versus HI, (**C**) TOC versus $S_1$, and (**D**) PI versus OSI.

Overall, the $Eh_3^6$ and $Eh_3^5$ shale studied herein exhibit only poor-to-fair oil potential, suggesting their limited contribution to oil reservoirs in the Biyang Depression. However, given the predominance of type $II_2$-III kerogen, it is hypothesized that these shales may possess significant gas potential in regions where wet/dry gas window maturity is attained. Notably, several gas fields have already been discovered near the Well A3 (Figure 1C). Considering the minimum OSI threshold (~100 mg HC/g TOC) for prospective shale oil successions in the lacustrine basins of China, [4] the studied $Eh_3^6$ and $Eh_3^5$ shale exhibit only minimal potential for shale oil exploration. Nevertheless, it is speculated that, in the central region of the paleo-lake, distant from the source area, there may be deposition of salinized lacustrine shale characterized by type I-$II_1$ kerogen and higher free oil contents. Therefore, the $Eh_3^6$ and $Eh_3^5$ shale around the Anpeng area, which was the sedimentary depocenter during the period, could represent a promising target for shale oil exploration.

## 6. Conclusions

The impact of terrigenous input on the deposition of salinized lacustrine shale was investigated using an example from the newly explored strata ($Eh_3^6$ and $Eh_3^5$) of the deep regions in the Biyang Depression, East China. The TOC contents of $Eh_3^6$ and $Eh_3^5$ shale range from 0.3 to 2.2 wt. %, with a predominance of type $II_2$-III kerogen. Both shale intervals exhibit a peak oil window maturity, as evidenced by vitrinite reflectance, $T_{max}$, and biomarker-derived maturity parameters. The primary source of OM is considered to be terrigenous higher plants for both shale intervals, supported by the dominance of terrigenous macerals (e.g., terrigenous liptinite, vitrinite, and inertinite), low HI values, and biomarker indicators. Additionally, a portion of the OM may originate from bacteria, as indicated

by the high abundance of hopanoids and the assignment of 7- and 8-methylheptadecanes. During the deposition of $Eh_3^6$ shale, a significant influx of detrital matter and terrigenous OM occurred, corresponding to high sediment accumulation rates (SARs). These high SARs facilitated the rapid burial of OM and increased paleosalinity by transporting salt ions from the provenance regions to the paleo-lake, thereby favoring OM preservation. Consequently, the $Eh_3^6$ shale, characterized by high TOC and low HI values, was deposited under the influence of high terrigenous OM input and favorable preservation conditions. In contrast, the deposition of $Eh_3^5$ shale involved a comparatively lower flux of detrital matter and terrigenous OM, resulting in shale with lower TOC and relatively higher HI values. Overall, the studied shale exhibits only poor-to-fair potential for hydrocarbon generation and retention. However, areas with higher maturity and a better kerogen type may hold significant potential for conventional gas and shale oil exploration in the Biyang Depression, respectively.

**Author Contributions:** Conceptualization and writing—original draft preparation, Y.S.; writing—review and editing, P.P.; funding acquisition, S.X.; project administration, S.J.; funding acquisition, B.G.; funding acquisition and methodology, S.L.; investigation, Q.C.; investigation, Z.L.; investigation, L.W.; investigation, C.L. All authors have read and agreed to the published version of the manuscript.

**Funding:** This research was funded by the general program of National Natural Science Foundation of China (Mechanism and prediction of fracture-induced by in situ heating of shale oil and oil shale reservoirs with different lithofacies), Open funding project of Sinopec Key Laboratory of Shale Oil/Gas Exploration and Production Technology (Reconstruction of biological community structure of organic-rich shale in saline lake basins and its quantitative indication of paleoproductivity), and National Natural Science Foundation of China (Grant Nos. 42072174, 42073067, and 41902139).

**Data Availability Statement:** The original contributions presented in the study are included in the article; further inquiries can be directed to the corresponding authors.

**Acknowledgments:** Henan Oilfield Company (SINOPEC) is gratefully appreciated for the permission of sampling.

**Conflicts of Interest:** The authors declare no conflicts of interest.

## References

1. Ruble, T.E.; Lewan, M.D.; Philp, R.P. New insights on the Green River petroleum system in the Uinta Basin from hydrous pyrolysis experiments. *AAPG Bull.* **2001**, *85*, 1333–1371. [CrossRef]
2. Zou, C.; Zhu, R.; Chen, Z.Q.; Ogg, J.G.; Wu, S.; Dong, D.; Qiu, Z.; Wang, Y.; Wang, L.; Lin, S.; et al. Organic-Matter-Rich shales of China. *Earth Sci. Rev.* **2019**, *189*, 51–78. [CrossRef]
3. Warren, J.K. Evaporites through time: Tectonic, climatic and eustatic controls in marine and nonmarine deposits. *Earth Sci. Rev.* **2010**, *98*, 217–268. [CrossRef]
4. Wang, M.; Guo, Z.; Jiao, C.; Lu, S.; Li, J.; Xue, H.; Li, J.; Li, J.; Chen, G. Exploration progress and geochemical features of lacustrine shale oils in China. *J. Pet. Sci. Eng.* **2019**, *178*, 975–986. [CrossRef]
5. Liu, B.; Song, Y.; Zhu, K.; Su, P.; Ye, X.; Zhao, W. Mineralogy and Element Geochemistry of Salinized Lacustrine Organic-Rich Shale in the Middle Permian Santanghu Basin: Implications for Paleoenvironment, Provenance, Tectonic Setting and Shale Oil Potential. *Mar. Pet. Geol.* **2020**, *120*, 104569. [CrossRef]
6. Liu, B.; Wang, H.; Fu, X.; Bai, Y.; Bai, L.; Jia, M.; He, B. Lithofacies and Depositional Setting of a Highly Prospective Lacustrine Shale Oil Succession from the Upper Cretaceous Qingshankou Formation in the Gulong Sag, Northern Songliao Basin, Northeast China. *AAPG Bull.* **2019**, *103*, 405–432. [CrossRef]
7. Hofmann, P.; Huc, A.Y.; Carpentier, B.; Schaeffer, P.; Albrecht, P.; Kelly, B.; Maxwell, J.R.; Damsté, J.S.S.; de Leeuw, J.W.; Leythaeuser, D. Organic matter of the Mulhouse Basin, France: A synthesis. *Org. Geochem.* **1993**, *20*, 1105–1123. [CrossRef]
8. Mascle, A.; Vially, R. The petroleum systems of the southeast basin and Gulf of Lion (France). *Geol. Soc.* **1999**, *156*, 121–140. [CrossRef]
9. Rodriguez, N.D.; Philp, R.P. Source Rock Facies Distribution predicted from oil geochemistry in the Central Sumatra Basin, Indonesia. *AAPG Bull.* **2015**, *99*, 2005–2022. [CrossRef]
10. Guo, P.; Liu, C.; Gibert, L.; Huang, L.; Zhang, D.; Dai, J. How to find high-quality petroleum source rocks in saline lacustrine basins: A case study from the Cenozoic Qaidam Basin, NW China. *Mar. Pet. Geol.* **2020**, *111*, 603–623. [CrossRef]
11. Xin, B.; Hao, F.; Han, W.; Xu, Q.; Zhang, B.; Tian, J. Paleoenvironment evolution of the lacustrine organic-rich shales in the second member of Kongdian Formation of Cangdong Sag, Bohai Bay Basin, China: Implications for organic matter accumulation. *Mar. Pet. Geol.* **2021**, *133*, 105244. [CrossRef]

12. Liang, C.; Jiang, Z.; Cao, Y.; Wu, J.; Wang, Y.; Hao, F. Sedimentary characteristics and origin of lacustrine organic-rich shales in the salinized Eocene Dongying Depression. *GSA Bull.* **2018**, *130*, 154–174. [CrossRef]
13. Kong, X.; Jiang, Z.; Zheng, Y.; Xiao, M.; Chen, C.; Yuan, H.; Chen, F.; Wu, S.; Zhang, J.; Han, C.; et al. Organic geochemical characteristics and organic matter enrichment of mudstones in an Eocene saline lake, Qianjiang Depression, Hubei Province, China. *Mar. Pet. Geol.* **2020**, *114*, 104194. [CrossRef]
14. Guan, M.; Liu, X.; Jin, Z.; Zhao, W.; Liu, W.; Bian, L.; Dong, J.; Zeng, X.; Zeng, B.; Sun, B.; et al. The formation of the Paleocene lacustrine organic-rich shale in the Subei Basin, East China Associated with the Early Late Paleocene event and marine incursions. *Mar. Pet. Geol.* **2024**, *162*, 106730. [CrossRef]
15. Song, Y.; Li, S.; Hu, S. Warm-humid paleoclimate control of salinized lacustrine organic-rich shale deposition in the Oligocene Hetaoyuan Formation of the Biyang Depression, East China. *Int. J. Coal Geol.* **2019**, *202*, 69–84. [CrossRef]
16. Xu, S.; Wang, Y.; Bai, N.; Wu, S.; Liu, B. Organic matter enrichment mechanism in saline lacustrine basins: A review. *Geol. J.* **2024**, *59*, 155–168. [CrossRef]
17. Li, S.; Hu, S.; Xie, X.; Lv, Q.; Huang, X.; Ye, J. Assessment of shale oil potential using a new free hydrocarbon index. *Int. J. Coal Geol.* **2016**, *156*, 74–85. [CrossRef]
18. Li, J.; Liu, Z.; Zhang, X.; Feng, G.; Liu, J.; Ma, Y.; Lu, S.; Li, W.; Zhou, N. Effects of paleoenvironment on continental shale oil enrichment and producibility in the Biyang Depression. *AAPG Bull.* **2022**, *106*, 2043–2071. [CrossRef]
19. Song, Y.; Cao, Q.; Li, S.; Hu, S.; Zhu, K.; Ye, X.; Wan, L. Salinized lacustrine organic-rich shale influenced by marine incursions: Algal-microbial community, paleoenvironment and shale oil potential in the Paleogene Biyang Depression, East China. *Palaeogeogr. Palaeoclimatol. Palaeoecol.* **2021**, *580*, 110621. [CrossRef]
20. Song, Y.; Wan, L.; Xu, S.; Gao, B.; Li, C.; Li, Z.; Paerzhana, P. Lake-level-fluctuation control on shale oil enrichment of the salinized lacustrine organic-rich shale in the Paleogene Biyang Depression, East China. *Minerals* **2024**, *14*, 94. [CrossRef]
21. Yuan, Y.Z.; Luo, J.Q.; Zhu, Y.; Liu, G.; Li, L.; Yu, M. Petroleum exploration history and enlightenment of Biyang Sag and Nanyang Sag in Nanxiang Basin. *Xinjiang Petro. Geol.* **2021**, *42*, 364–373, (In Chinese with English abstract).
22. Dong, Y.; Zhu, X.; Xian, B.; Hu, T.; Geng, X.; Liao, J.; Luo, Q. Seismic Geomorphology Study of the Paleogene Hetaoyuan Formation, Central-South Biyang Sag, Nanxiang Basin, China. *Mar. Pet. Geol.* **2015**, *64*, 104–124. [CrossRef]
23. Xu, K.; Chen, H.; Huang, C.; Ogg, J.G.; Zhu, J.; Lin, S.; Yang, D.; Zhao, P.; Kong, L. Astronomical Time Scale of the Paleogene Lacustrine Paleoclimate Record from the Nanxiang Basin, Central China. *Palaeogeogr. Palaeoclimatol. Palaeoecol.* **2019**, *532*, 109253. [CrossRef]
24. Taylor, G.H.; Teichmüller, M.; Davis, A.; Diessel, C.F.K.; Littke, R.; Petrology, P.R. RobertOrganic Petrology. In *A New Handbook Incorporating Some Revised Parts of Stach's Textbook of Coal Petrology*; Gebrüder Borntraeger: Berlin, Stuttgart, 1998; Geological Magazine; Volume 136, pp. 697–711. ISBN 3–443–01036–9.
25. Shen, J.; Schoepfer, S.D.; Feng, Q.; Zhou, L.; Yu, J.; Song, H.; Wei, H.; Algeo, T.J. Marine Productivity Changes during the End-Permian Crisis and Early Triassic Recovery. *Earth Sci. Rev.* **2015**, *149*, 136–162. [CrossRef]
26. Tribovillard, N.; Algeo, T.J.; Riboulleau, A. Trace metals as paleoredox and paleoproductivity proxies: An update. *Chem. Geol.* **2006**, *232*, 12–32. [CrossRef]
27. Rudnick, R.L.; Gao, S. Composition of the continental crust. In *Treatise on Geochemistry*, 2nd ed.; Newnes: Boston, UK, 2014; pp. 1–51.
28. Cassani, F.; Gallango, O.; Talukdar, S.; Vallejos, C.; Ehrmann, U. Methylphenanthrene maturity index of marine source rock extracts and crude oils from the Maracaibo Basin. *Org. Geochem.* **1988**, *13*, 73–80. [CrossRef]
29. Radke, M.; Welte, D.H.; Willsch, H. Maturity Parameters Based on Aromatic Hydrocarbons: Influence of the Organic Matter Type. *Org. Geochem.* **1986**, *10*, 51–63. [CrossRef]
30. Peters, K.E.; Walters, C.C.; Moldowan, J.M. *The Biomarker Guide: Column 2, Biomarkers and Isotopes in Petroleum Systems and Earth History*, 2nd ed.; Cambridge University Press: Cambridge, UK, 2005.
31. Hanson, A.D.; Zhang, S.C.; Moldowan, J.M.; Liang, D.G.; Zhang, B.M. Molecular organic geochemistry of the Tarim Basin, northwest China. *AAPG Bull.* **2000**, *84*, 1109–1128.
32. Volkman, J.K.; Allen, D.I.; Stevenson, P.L.; Burton, H.R. Bacterial and algal hydrocarbons from a saline Antarctic lake, Ace Lake. *Org. Geochem.* **1986**, *10*, 671–681. [CrossRef]
33. Volkman, J.K.; Barrett, S.M.; Blackburn, S.I. Eustigmatophyte microalgae are potential sources of C29 sterols, C22–C28 n-alcohols and C28–C32 n-alkyl diols in freshwater environments. *Org. Geochem.* **1999**, *30*, 307–318. [CrossRef]
34. Otto, A.; Wilde, V. Sesqui-, di-, and triterpenoids as chemosystematic markers in extant conifers; a review. *Bot. Rev.* **2001**, *67*, 141–238. [CrossRef]
35. Ourisson, G.; Albrecht, P.; Rohmer, M. The hopanoids: Palaeochemistry and biochemistry of a group of natural products. *Pure Appl. Chem.* **1979**, *51*, 709–729. [CrossRef]
36. Rohmer, M.; Bisseret, P.; Neunlist, S. The hopanoids, prokaryotic triterpenoids and precursors of ubiquitous molecular fossils. In *Biological Markers in Sediments and Petroleum*; Moldowan, J.M., Albrecht, P., Philp, R.P., Eds.; Prentice Hall: Englewood Cliffs, NJ, USA, 1992; pp. 1–17.
37. Shiea, J.; Brassell, S.C.; Ward, D.M. Mid-chain branched mono- and dimethyl alkanes in hot spring cyanobacterial mats: A direct biogenic source for branched alkanes in ancient sediments? *Org. Geochem.* **1990**, *15*, 223–231. [CrossRef]

38. Wei, W.; Algeo, T.J. Elemental proxies for paleosalinity analysis of ancient shales and mudrocks. *Geochim. Cosmochim. Acta* **2020**, *287*, 341–366. [CrossRef]
39. Didyk, B.M.; Simoneit, B.R.T.; Brassell, S.C.; Eglinton, G. Organic geochemical indicators of paleoenvironmental conditions of sedimentation. *Nature* **1978**, *272*, 216–222. [CrossRef]
40. Asif, M.; Alexander, R.; Fazeelat, T.; Pierce, K. Geosynthesis of dibenzothiophene and alkyl dibenzothiophenes in crude oils and sediments by carbon catalysis. *Org. Geochem.* **2009**, *40*, 895–901. [CrossRef]
41. Algeo, T.J.; Tribovillard, N. Environmental analysis of paleoceanographic systems based on molybdenum–uranium covariation. *Chem. Geol.* **2009**, *268*, 211–225. [CrossRef]
42. Schoepfer, S.D.; Shen, J.; Wei, H.; Tyson, R.V.; Ingall, E.; Algeo, T.J. Total organic carbon, organic phosphorus, and biogenic barium fluxes as proxies for paleomarine productivity. *Earth Sci. Rev.* **2015**, *149*, 23–52. [CrossRef]
43. Rosen, M. The importance of groundwater in playas: A review of playa classifications and the sedimentology and hydrology of playas. *GSA Bull.* **1994**, *289*, 1–18.
44. Peters, K.E. Guidelines for petroleum source rock using programmed pyrolysis. *AAPG Bull.* **1986**, *70*, 318–329.


**Disclaimer/Publisher's Note:** The statements, opinions and data contained in all publications are solely those of the individual author(s) and contributor(s) and not of MDPI and/or the editor(s). MDPI and/or the editor(s) disclaim responsibility for any injury to people or property resulting from any ideas, methods, instructions or products referred to in the content.